42nd AIAA Plasmadynamics and Lasers Conference
 in conjunction with the
 18th Internati
27 - 30 June 2011, Honolulu, Hawaii

AIAA 2011-3282

Recent AAOL In-Flight Wavefront Measurements of Aero-Optics and Implications for Aero-Optics Beam Control in Tactical Laser Weapon Systems

David J. Goorskey [*] , Matthew R. Whiteley [†]
MZA Associates, Dayton, OH, 45430

Stanislav Gordeyev [‡] , Eric J. Jumper [§]
Center for Flow Physics and Control
University of Notre Dame, Notre Dame, IN, 46556

Aero-optics disturbances were measured *in-flight* with the Airborne Aero-Optics Laboratory (AAOL) 1 ft (4 in. clear aperture) flat-windowed turret at an altitude of 15 kft altitude and at a Mach number of 0.5 for 47^o az., 42^o el. (forward-looking) and 139^o az., 70^o el. (rear-looking) turret angles. Wavefronts were collected using a FasCam CCD array camera with an AMO lenslet array in a Shack-Hartman configuration at a 20 kHz frame-rate. 2,000 consecutive wavefronts of each of the two turret pointing angles measured were scaled to a tactical high energy laser (HEL) laser weapon scenario and their wavefront error statistics analyzed. The two wavefront sequences were decomposed using proper orthogonal decomposition (POD) modes and their spatial frequency content evaluated. From this, the minimum number of deformable mirror (DM) actuators needed to compensate these disturbances was estimated to be approximately 18 actuators across the aperture diameter. Finally, a the performance of a simple integrator-type adaptive optics (AO) control system against the two scaled wavefront sequences was investigated. It was found that the forward-looking aero-optics aberrations were about three-times less in magnitude than the rear-looking aero-optics aberrations. Consequently, the open-loop Strehl ratio of the forward-looking case was considerably greater than the open-loop Strehl ratio of the rear-looking case. Nevertheless, in for both the forward-looking and rear-looking cases, in order to achieve compensation better than open-loop, it was found necessary to have AO sample rates greater than 10 kHz with one frame of latency. These results suggest that significant AO compensation improvements will be achieved mainly by reducing the latency as much as possible, perhaps with adaptive/predictive AO controllers.

Nomenclature

α, β, γ	Turret azimuth, elevation, and window angles, respectively
D_t	Turret outer diameter
D'_t	New turret outer diameter
D_{ap}	Turret clear aperture diameter
h_t	Turret base height
Φ	Wavefront
Φ'	Scaled wavefront
Φ^{ND}	Non-dimensionalized wavefront
f	Temporal frequency
f'	Scaled temporal frequency
f^{ND}	Non-dimensionalized temporal frequency

[*]Scientist, MZA Dayton Operations, Member AIAA.
[†]Vice President, Senior Scientist, MZA Dayton Operations, Member AIAA.
[‡]Research Assistant Professor, Department of Aerospace and Mech. Eng., Member AIAA.
[§]Professor, Department of Aerospace and Mech. Eng., Fellow AIAA.

f_s	Sampling frequency of adaptive optics system
X	Transverse spatial quantity
X'	Scaled transverse spatial quantity
X^{ND}	Non-dimensionalized transverse spatial quantity
M	Mach number
M'	New Mach number
ρ	Air density at altitude
ρ'	New air density at new altitude
ρ_{SL}	Air density at sea level, 1.225 kg/m^3
v_p	Platform velocity
v_p'	New platform velocity
v_s	Velocity of sound
Γ_A	Ratio of specific heat of air at constant pressure to heat at constant volume
P	Air pressure at altitude
K_{GD}	Gladstone-Dale constant
K_{GD}'	New Gladstone-Dale constant
n	Index of refraction
n_o	Non-varying index of refraction part
OPL	Optical path length
λ	Wavelength of light
λ'	New wavelength of light
ρ_0	Non-varying density part
$\Delta\rho$	Varying density part
$\Delta\rho'$	New varying density part
ds	Incremental optical path length
S	Optical path
OPD	Optical path difference
POD_i	ith Proper Orthogonal Decomposition (POD) mode
$\boldsymbol{K}$	Matrix of vectorized wavefronts
N_x	Number of wavefronts
N_m	Number of POD modes
$\boldsymbol{x}_i$	Vectorized form of ith wavefront
$\boldsymbol{U}$	Left matrix of singular value decomposition of $\boldsymbol{K}$
$\boldsymbol{\Sigma}$	Center matrix of singular value decomposition of $\boldsymbol{K}$
$\boldsymbol{V}^T$	Right matrix of singular value decomposition of $\boldsymbol{K}$
$\boldsymbol{K}$	Matrix of POD coefficients ($= \boldsymbol{U\Sigma}$)
Φ_i	Temporal power spectral density (PSD) of ith POD mode
Φ_i^{CL}	Closed-loop temporal power spectral density (PSD) of ith POD mode
Φ_i^{OL}	Open-loop temporal power spectral density (PSD) of ith POD mode
ERJ	Error rejection function of adaptive optics system
β	Closed-loop gain of adaptive optics system
Δt	Closed-loop latency (# frames) of adaptive optics system
St	Strehl ratio
rms	Root mean square
WFE	Wavefront error
σ	Total rms wavefront error
σ_i	rms wavefront error of ith POD mode
Ψ_i	2D spatial power spectrum of ith POD mode
Ψ_i^{rad}	Radial spatial power spectrum of ith POD mode
ν_r	Radial spatial frequency
$\nu_{r,i}^{max}$	Radial spatial frequency which contains 80% of the total wavefront variance of the ith POD mode
ν_θ	Angular spatial frequency
$\boldsymbol{\mathcal{F}}_{2D}$	2D discrete Fourier transform
x, y	Cartesian spatial coordinates transverse to optical axis
θ	Angular spatial coordinate in plane transverse to optical axis

$N_{act,k}^{min}$ Number of DM actuators across aperture required to compensate up to k number of POD modes

I. Introduction

Currently, much attention is being paid toward the effects of aero-optics on airborne tactical HEL weapon systems. Until recently the only available experimental wavefront measurements of aero-optics disturbances has come from wind-tunnel tests. One of the goals of the AAOL program, funded by Air Force Office of Scientific Research (AFOSR), is to collect wavefront measurements *in-flight* at transonic/near-transonic conditions for a wide range of turret pointing angles, altitudes, and Mach numbers. The AAOL program uses two Cessna Citations that fly in formation at about 45-75 m separation with one aircraft carrying the probe laser and the second aircraft carrying the flat-windowed AAOL turret (which protrudes out the side of the Citation cabin door) that receives the probe laser after it passes through the turbulent boundary layer of the second aircraft. Thus, for different flying conditions and turret pointing angles, a better understanding of the aero-optics around turrets in actual flight can be obtained. Here, analysis of recent AAOL in-flight wavefront measurements, carried out in February 2011, are presented and the potential implications for AO beam control for tactical HEL weapon systems discussed.

A. Test conditions

Wavefronts were collected *in flight* at 15 kft altitude and at Mach 0.5 using a green 532 nm laser with the 1 ft diameter AAOL turret and a 4 in. flat aperture. Figure 1 shows a plot of the rms wavefront error (in non-dimensionalized form) for the various turret window angles measured.

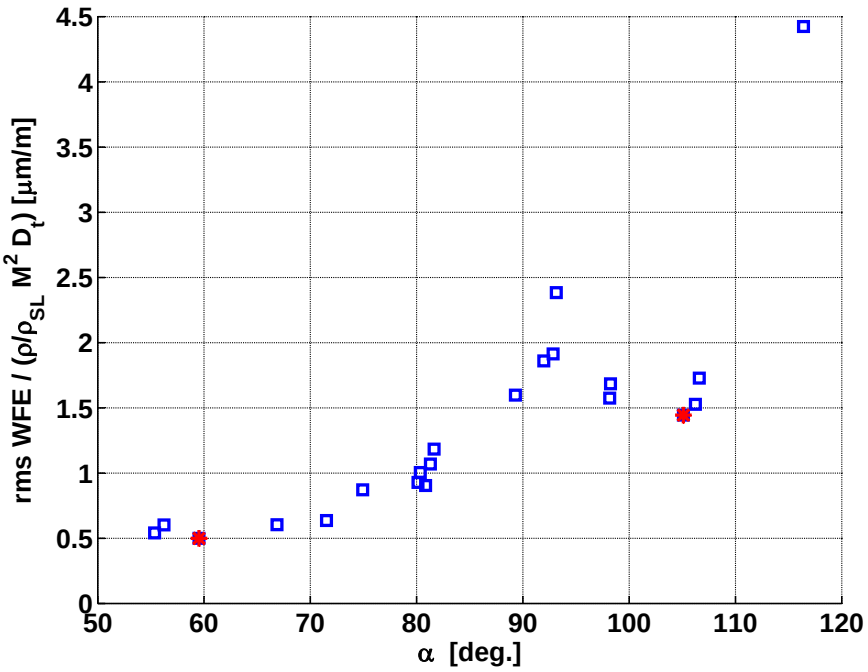

Figure 1. Wavefront error of February 2011 AAOL flight test measurements versus turret window angle.

In this paper, we chose two turret window angles (marked by a red "*" in Figure 1) that are representative of different aero-optic flow regimes to examine in more detail and assess the ability of an AO system to compensate these aberrations:

- 47^o az., 42^o el. (60^o turret window angle)
- 139^o az., 70^o el. (105^o turret window angle)

Although nearly 8,000 wavefront frames were collected for each data set above, for the purposes of the analysis reported here, only 2,000 consecutive frames of each wavefront sequence were used.

B. Collection method

Wavefronts were collected using a **FasCam** CCD array camera (512 × 512 pixels at up to 20 kHz frame rate, 20 μm pitch, TIFF images) with an **AMO** lenslet array (21.3 × 18 mm, 71 × 60 lenslets, 0.3 mm/lenslet pitch, 38.2 mm focal length) in a Shack-Hartman configuration. The collection frame rate for the wavefront sequences presented here was 20 kHz. Wavefront reconstruction was carried out using the iterative Southwell method of the **AMO/Wavefront Sciences** wavefront sensor software.

C. Preprocessing of raw wavefronts

After raw wavefronts were collected and reconstructed, the following 2D wavefront data reduction procedure was followed:

- A reference "no-flow" wavefront was obtained at the beginning of each run to absorb all non-flow related aberrations imposed on the laser beam and all wavefronts were measured as deviations from this reference wavefront.
- A steady (mean lensing) wavefront was computed by averaging among all wavefronts.
- The steady (mean lensing) wavefront was subtracted from each wavefront to yield only instantaneous wavefronts.
- Piston and tip/tilt components were removed from each wavefront. The removed tip/tilt was recorded and mean values of the removed tip/tilt were calculated.

II. Analysis Procedures

A. Geometry

In order to avoid confusion, it is beneficial at the onset to define the turret geometry so that there will be no confusion in the understanding of azimuth and elevation angles as well as flow direction over the aperture. Figure 2 shows the turret pointing angles with respect to the flow direction. α and β are the azimuth and elevation angles, respectively. The turret window angle, γ is calculated from the azimuth and elevation angles by the equation:

$$\cos\gamma = \cos\alpha\cos\beta. \tag{1}$$

The wavefronts presented and analyzed here are given in the aperture frame of reference, i.e. as if looking out through the aperture.

B. Altitude, Mach Number, and Turret Diameter Scaling

The proposed scaling relations between wavefronts at different altitudes, Mach numbers, and turret diameters (for the same azimuth and elevation angles) are given by the following:[1,2,3,4]

$$\phi' = \left(\frac{\rho'}{\rho}\right)\left(\frac{M'}{M}\right)^2\left(\frac{D_t'}{D_t}\right)\phi \tag{2}$$

$$f' = \left(\frac{v_p'}{v_p}\right)\left(\frac{D_t}{D_t'}\right)f \tag{3}$$

$$X' = \left(\frac{D_t'}{D_t}\right)X, \tag{4}$$

where the "primed" quantities are at the new altitude, Mach number, and turret diameter and the "unprimed" quantities are at the old altitude, Mach number, and turret diameter. ϕ is the wavefront in [m]. ρ is the air density at altitude. M is the Mach number of the platform. D_t is the turret diameter in [m]. f is the sample rate in [Hz]. Time is, of course, scaled inversely to f. v_p is the speed of the platform. X is any spatial quantity

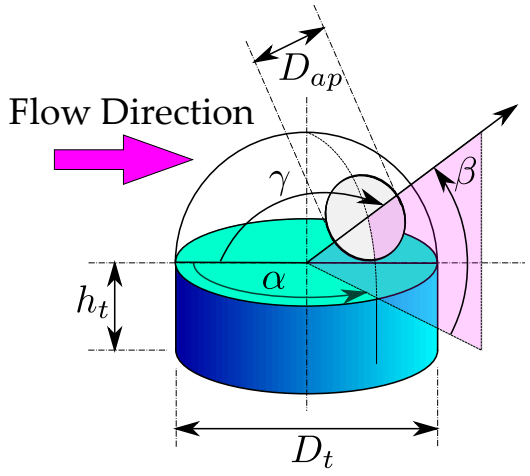

Figure 2. Turret pointing angles with respect to flow direction. α is the azimuth angle. β is the elevation angle. γ is the window angle. D_t is the turret diameter. D_{ap} is the aperture diameter. h_t is the turret base height.

such as pixel (subaperture) spacing dxy, aperture diameter D_{ap}, or obscuration diameter D_{ob}. Often it is useful to present wavefront analysis results in non-dimensional quantities for easy scaling to any relevant application. To do so, we first *non-dimensionalize* the wavefronts according to the following:

$$\phi^{ND} = \left(\frac{1}{\frac{\rho}{\rho_{SL}} M^2 D_t}\right) \phi \tag{5}$$

$$f^{ND} = \left(\frac{D_t}{v_p}\right) f \tag{6}$$

$$X^{ND} = \left(\frac{1}{D_t}\right) X, \tag{7}$$

where ρ_{sL} is the density of air at sea level (1.225 kg/m^3). Then, to scale to any other altitude, Mach number, and turret diameter, we *dimensionalize* according to the following:

$$\phi' = \left(\frac{\rho'}{\rho_{SL}} M'^2 D'_t\right) \phi^{ND} \tag{8}$$

$$f' = \left(\frac{v'_p}{D'_t}\right) f^{ND} \tag{9}$$

$$X' = (D'_t)\, X^{ND}. \tag{10}$$

For a given altitude, we calculate the air density (ρ) and air pressure (P) from the *U.S. Standard 1976* model. Then, from these quantities, we arrive at the speed of sound at altitude:

$$v_s = \sqrt{\Gamma_A P/\rho}, \tag{11}$$

where $\Gamma_A = 1/4$. Using the speed of sound at altitude we get the platform speed according to the relation:

$$v_p = M v_s. \tag{12}$$

C. Wavelength Scaling

Although not included as part of the non-dimensionalization discussed in Section B above, scaling with wavelength is necessary when the wavefronts are measured at one wavelength and the application scenario

involves a different wavelength. The wavelength scaling relation is derived as follows. First, the optical path length (OPL) is

$$OPL = \int_S n\, ds. \tag{13}$$

The integral is over some path S of which ds is an incremental step. In general, we can write the index of refraction n as

$$n = n_0 + n_1, \tag{14}$$

where n_0 is the non-varying part and n_1 is the varying part over the path. The the index of refraction is proportional to the air density ρ through the relation:

$$n = 1 + K_{GD}\rho, \tag{15}$$

where K_{GD} is the Gladstone-Dale constant. In general the Gladstone-Dale constant varies with wavelength λ as[5]

$$K_{GD} = 2.23 \times 10^{-4}\left(1 + \frac{7.52 \times 10^{-15}}{\lambda^2}\right). \tag{16}$$

Expressing the density ρ as a sum of non-varying ρ_0 and varying $\Delta\rho = \rho - \rho_0$ parts over the path

$$\rho = \rho_0 + \Delta\rho, \tag{17}$$

the relation of Eq. (15) becomes

$$\begin{aligned} n &= 1 + K_{GD}\left(\rho_0 + \Delta\rho\right) && (18)\\ &= 1 + K_{GD}\rho_0 + K_{GD}\Delta\rho && (19)\\ &= n_0 + K_{GD}\Delta\rho, && (20) \end{aligned}$$

where $n_0 = 1 + K_{GD}\rho_0$.

The optical path difference (OPD) is defined to be only the path-fluctuating part of the the OPL, so we have

$$OPD = \phi = \int_S K_{GD}\Delta\rho\, ds. \tag{21}$$

Given that we are interested in the wavelength scaling relationship between new ϕ' and old ϕ OPDs, we note that although K_{GD} is wavelength-dependent it is path-independent and so can be brought out of the path integral to yield:

$$\frac{\phi'}{\phi} = \frac{K'_{GD}\int_S \Delta\rho'\, ds}{K_{GD}\int_S \Delta\rho\, ds}. \tag{22}$$

With all else equal over the path, *i.e.* the only scaling is respect to wavelength, $\Delta\rho' = \Delta\rho$ and so we end up with the wavelength scaling relationship:

$$\phi' = \frac{K_{GD}(\lambda')}{K_{GD}(\lambda)}\phi, \tag{23}$$

where λ' is the new wavelength and λ is the old wavelength.

D. Proper Orthogonal Decomposition

Most of the subsequent analysis is conducted by first decomposing the individual wavefronts over a set of orthogonal modes. While the conventional approach in dealing with atmospheric turbulence has been to use Zernike modes, we have found that Zernike modes are not suited to the types of aero optics disturbances studied here. Zernike modes are most suited to aberrations that possess some radial symmetry. With aero optics, especially at larger azimuth angles, this is most definitely not the case. Therefore, we choose instead to work with a set of modes derived directly from the data itself called POD modes.[6,7,8,9,10,11] POD modes are identical to the Karhunen-Loev modes and modes from Principal Component Analysis (PCA). Essentially, POD modes are ordered according to their modal variance. Thus the first mode has the greatest disturbance and the second mode has the second greatest disturbance, etc.. Furthermore, the modes are statistically independent of each other, unlike Zernike modes, which are orthogonal, but not statistically independent.

Finding the POD modes is a relatively easy task. Suppose we have N_x wavefronts of size $m \times n$ pixels. We reshape each wavefront into a vector form so that now we have N_x column vectors $\boldsymbol{x}_i$ of length mn. Group these vectorized wavefronts $\boldsymbol{x}_i$ into one matrix $\boldsymbol{K}$ as follows:

$$\boldsymbol{K} = [\boldsymbol{x}_1 \ \boldsymbol{x}_2 \ \boldsymbol{x}_3 \ \ldots \ \boldsymbol{x}_{N_x}]. \tag{24}$$

Then we do a singular value decomposition on the matrix $\boldsymbol{K}$ to get

$$\boldsymbol{K} = \boldsymbol{U}\boldsymbol{\Sigma}\boldsymbol{V}^T. \tag{25}$$

We define

$$\boldsymbol{Q} = \boldsymbol{U}\boldsymbol{\Sigma}. \tag{26}$$

Then we have

$$\boldsymbol{K} = \boldsymbol{Q}\boldsymbol{V}^T. \tag{27}$$

The *columns* of $\boldsymbol{V}^T$ are the POD modes in vectorized form. The *rows* of $\boldsymbol{Q}$ are the POD coefficients. If we include N_m modes, then $\boldsymbol{Q}$ is size $[N_x \times N_m]$ and $\boldsymbol{V}^T$ is size $[N_m \times mn]$. In order to visualize the POD modes easier, we reshape them back into 2-D form with size $[m \times n]$. The important thing to remember about POD modes are that they are not independent of the data. Different data sets give different POD modes, although if the underlying spatial and temporal statistics of two data sets are similar, their POD mode sequences will be similar.

E. Assessing conventional AO compensation performance and requirements

Using the POD modes from a measured wavefront sequence that is scaled to a particular application scenario, we would like to be able to assess the ability of a conventional AO control system to mitigate such disturbances with different frame rates, latencies, and closed loop gains. In particular, we would like to use these assessments to determine a set of minimum spatial and temporal requirements for a conventional AO control system for effective aero-optics compensation.

The basic procedure we follow is to first decompose the scaled wavefront sequence into POD modes. For each POD mode, there is a time history of POD modal coefficients. From these POD modal coefficients, we calculate the temporal power spectra of each POD mode. Then, we apply a theoretical error rejection function for a conventional controller to each modal power spectrum as such:

$$\Phi_i^{CL}(f) = ERJ(f) \times \Phi_i^{OL}(f), \tag{28}$$

where $\Phi_i^{OL}(f)$ and $\Phi_i^{CL}(f)$ are the power spectral densities (PSDs) of the i^{th} POD mode before (open-loop) and after compensation (closed-loop), respectively. $ERJ(\omega)$ is the error rejection function of a conventional AO controller (simple integrator type) given by:

$$ERJ(f; f_s, \beta, \Delta t) = \left[1 + \left(\frac{\beta f_s}{2\pi f}\right)^2 - 2\left(\frac{\beta f_s}{2\pi f}\right)\sin(2\pi f \Delta t)\right]^{-1}. \tag{29}$$

where f_s is the sample rate, β is the closed loop gain, and Δt is the latency.

From this we can calculate modal Strehl ratios (St_i) using the Marèchal approximation:

$$St_i = exp\left[-\left(\frac{2\pi\sigma_i}{\lambda}\right)^2\right], \tag{30}$$

where the modal variance, σ_i^2 is given by:

$$\sigma_i^2 = \sum_{j=1}^{N_f} \Phi_i(f_j) \times df. \tag{31}$$

The sum in Eq. (31) is carried out over all N_f discrete frequencies of the POD modal PSDs and df is the frequency spacing.

The total Strehl ratio (St) is given by the following:

$$St = exp\left[-\left(\frac{2\pi\sigma}{\lambda}\right)^2\right], \tag{32}$$

where the total variance, σ^2 is calculated by summing all N_m POD modal variances according to:

$$\sigma^2 = \sum_{i=1}^{N_m} \sigma_i^2. \tag{33}$$

Using the above procedure, we evaluate the effectiveness of a conventional AO system against a sequence of aero-optics wavefronts scaled to a specific application scenario by varying the controller sample rate f_s, loop gain β, and latency Δt parameters and computing the resulting total Strehl ratio St and residual wavefront error σ.

In order to the minimum spatial requirements of an AO system, we first take the 2D discrete Fourier transform of each POD mode. These can be thought of as POD modal spatial power spectra, or PSDs:

$$\Psi_i(\nu_r, \nu_\theta) = \boldsymbol{\mathcal{F}}_{2D}\left[POD_i(x, y)\right], \tag{34}$$

where $\Psi_i(\nu_r, \nu_\theta)$ is the spatial PSD of the i^{th} POD mode. ν_r and ν_θ are the spatial radial and angular frequencies, respectively. $\boldsymbol{\mathcal{F}}_{2D}$ denotes the 2D discrete Fourier transform. We then take 360 radial "slices" of each of the POD spatial PSDs, one for each angular degree, and we average them together to form just one radial spatial PSD for each POD mode:

$$\Psi_i^{rad}(\nu_r) = \sum_{\theta=0^o}^{359^o} \Psi_i(\nu_r, \nu_\theta)/360. \tag{35}$$

These POD radial spatial PSDs usually consist of a major peak. We have found that with increasing POD mode number, the POD radial spatial PSD peak shifts to higher radial spatial frequency. We take the cumulative sum of the normalized POD radial spatial PSDs $\Psi_i^{rad}(\nu_r)$ and find the radial spatial frequency value $\nu_{r,i}^{max}$ at which the cumulative sum is 80% of the total sum:

$$\sum_{\nu_r}^{\nu_{r,i}^{max}} \Psi_i^{rad}(\nu_r) = 0.80 \sum_{\nu_r} \Psi_i^{rad}(\nu_r) \tag{36}$$

Thus, we end up with an upper bound on the radial spatial frequency content present in each POD mode. Using this, we can estimate a minimum number of actuators across the turret aperture that would be required to compensate up to k number of POD modes:

$$N_{act,k}^{min} \approx 2\nu_{r,k}^{max} D_{ap}. \tag{37}$$

III. Analysis and Results

In the following subsections, the AAOL-measured wavefronts were scaled to a relevant tactical airborne HEL weapon system application scenario: Mach 0.5, 25 kft, 30 cm aperture diameter, and 90 cm turret diameter.

A. Mach 0.5, 15 kft, $\alpha = 60^o$ (47^o az., 42^o el.)

1. Wavefront error

Wavefront error statistics for the original (as-measured) wavefronts, non-dimensionalized wavefronts, and wavefronts scaled to the application scenario above are given in Table 1. The "Ap. Avg. Phase Var." is computed by taking the variance of each pixel over all the frames ("ensemble" variance) and averaging over all pixels within the aperture (and not within the central obscuration area). The "rmsWFE" is computed by taking the square root of the aperture-averaged phase variance. The "Avg. OPDrms" is computed by the rms deviation of each wavefront from zero and averaging over all wavefronts in the sequence. The "Avg. OPDp-v" is computed by averaging the peak-to-valley of each wavefront over all wavefronts in the sequence. The non-dimensionalized wavefronts are unitless and so the wavefront error statistical quantities are likewise unitless.

	As Measured	Non-Dimensionalized	Scaled to Application
Ap. Avg. Phase Var. [μm^2]	0.001	0.249	0.002
rms WFE [μm]	0.024	0.499	0.049
avg. OPDrms [μm]	0.023	0.494	0.049
avg. OPDp-v [μm]	0.159	3.341	0.331

Table 1. Wavefront error statistics for 15 kft, Mach 0.5, 47^o az., 42^o el.. Units are for "As-Measured" and "Scaled to Application" wavefronts only. Non-dimensionalized wavefronts are unitless.

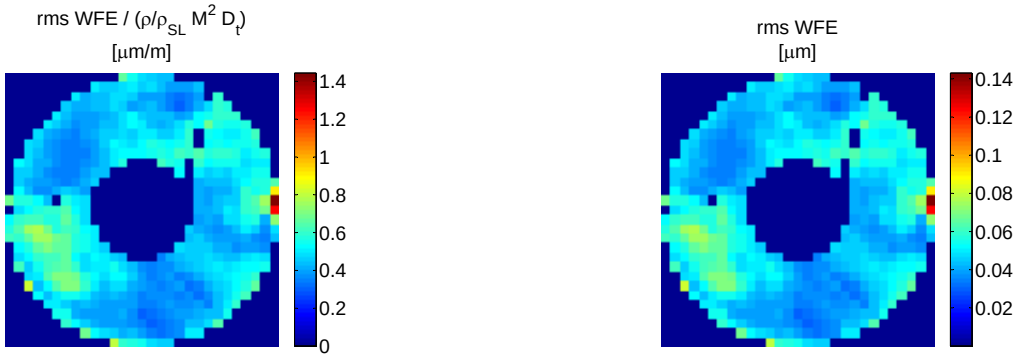

(a) (b)

Figure 3. Ensemble root-mean-square wavefront error (rmsWFE) on a pixel-by-pixel basis for (a) non-dimensionalized wavefronts and (b) wavefronts scaled to the application scenario.

Figure 3 shows the ensemble rms deviation of each pixel from zero for both (a) non-dimensionalized wavefronts and (b) wavefronts scaled to the Electric Laser on Large Aircraft (ELLA)-relevant application. For forward-looking turret window angles such as this one, the flow direction is not readily apparent since the aberrations lack a unified flow direction.

We can get a general idea of the frequency content of this wavefront sequence by calculating the power spectrum of each pixel and then averaging them together over all the wavefront frames to get a aperture-averaged pixel power spectral density (PSD). Figure 4 shows (a) the aperture-averaged pixel PSD and (b) cumulative sum of aperture-averaged pixel PSD. Notice that the left and bottom axis are in non-dimensionalized units while the right and top axis are units corresponding to the wavefronts scaled to the application.

2. POD modal analysis

The first 10 POD modes are depicted in Figure 5. The white areas are the areas of the wavefronts which were not used due to the central obscuration of the telescope's secondary mirror.

Figure 6(a) is a plot of the rms wavefront error of each POD mode. Since POD modes are ranked, or ordered, according to the level of variation, or energy, content in each mode, the rms wavefront error of each POD mode becomes progressively weaker with increasing mode number. A cumulative sum of the POD rms wavefront errors is shown in Figure 6(b). As expected the cumulative POD rms wavefront error quickly approaches the total rms wavefront error. For comparison, the cumulative Zernike rms wavefront error is also plotted. However, the Zernike rms wavefont undershoots the total rms wavefront error, meaning that the Zernikes are not an appropriate basis set for aero-optics wavefront decomposition. This can be qualitatively understood by examining the POD modes in Figure 5. There is very little radial symmetry present and because the Zernike modes are radially symmetric, they do not offer a good representation of the dominant variational structures present in aero-optics disturbances.

The POD coefficients are used to generate PSDs, one for each POD mode. Figure 7(a) shows a plot of the first four POD PSDs. Figure 7(b) shows a plot of the cumulative sums of the first seven POD PSDs. As stated earlier in Section E, the POD PSDs are used to assess the performance of a simple integrator type conventional AO controller against these disturbances.

3. Spatial frequency content

In order to quantify the spatial frequency content of these aero-optics disturbances, we follow the procedure outlined in Section E. Figure 8(a) shows an example of a normalized radial spatial PSD for the 150^{th} POD mode $\Psi_{150}^{rad}(\nu_r)/max(\Psi_{150}^{rad}(\nu_r))$. The maximum spatial frequency content as function of POD mode number $\nu_{r,k}^{max}$ is shown in Figure 8(b). $\nu_{r,k}^{max}$ is defined to be the spatial frequency which contains 80% of the total area under the radial spatial PSD for mode k. From this we can estimate that the number of actuators needed to compensate up to 100 POD modes, for example, would be $2 \times \nu_{r,100}^{max} = 2 \times 9 = 18$ actuators across the aperture.

4. Conventional AO compensation performance

In this section we present the results of applying a theoretical error rejection function for a conventional, simple-integrator type AO controller to the POD PSDs as outlined in Section E. Figure 9 shows the result of a zero-latency, 0.5 gain conventional AO controller in terms of Strehl (right axis, blue curve) and normalized residual rms wavefront error (left axis, black curve). This plot is used to get an estimate of the minimum sample rate $f_{s,min}$ needed for effective compensation which we define to be the sample rate at which the rms wavefront error is reduced by half. For this wavefront sequence, even a low frequency AO system results in a Strehl ratio greater than 0.9.

Next, we move on to looking at conventional AO controller performance with different latencies, sample rates, and gains. These results are shown in Figure 10 and Figure 11. From these plots, one can get an idea as to the requirements of a conventional AO controller that should be met in order to achieve a specific level of aero-optics mitigation. For example, if we have a 1 frame of latency system, the maximum Strehl we can achieve would be above 90% with a gain of close to 0.4 and a sample rate of 20 kHz. See Figure 10(d). Since the forward-looking aero-optics aberrations are not that strong to begin with, for lower sample rates, open-loop is better than closed-loop. As expected, if the loop latency is reduced, the Strehl improves slightly.

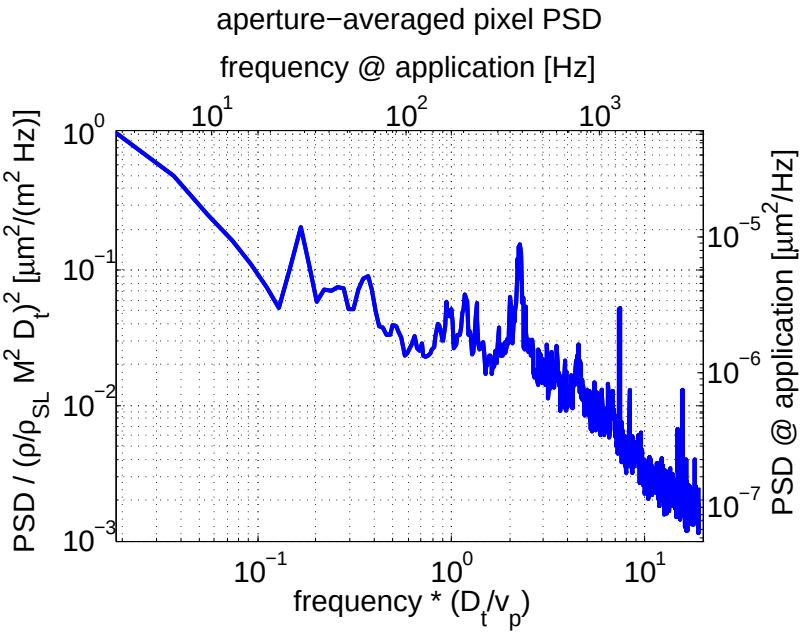

(a)

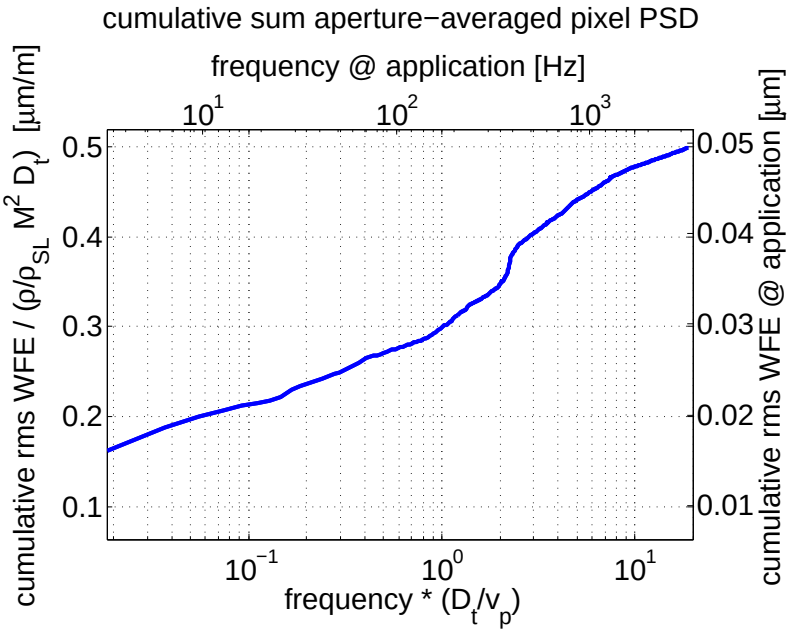

(b)

Figure 4. (a) Aperture-averaged pixel PSD. (b) Cumulative aperture-averaged pixel PSD.

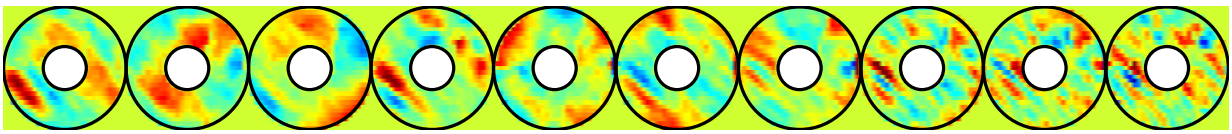

Figure 5. First 10 POD modes.

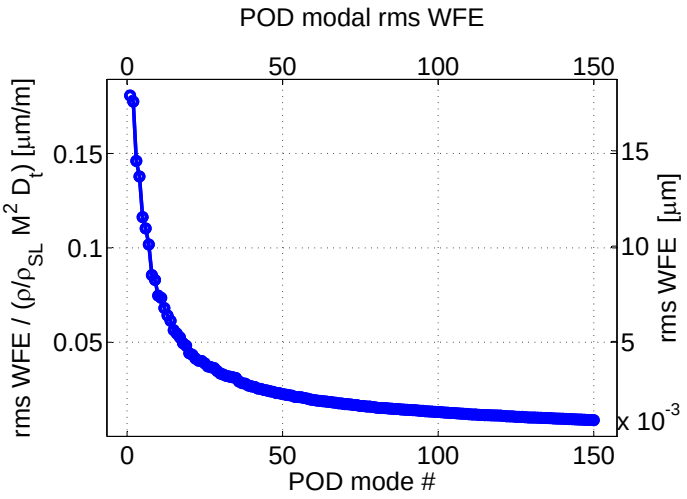

(a)

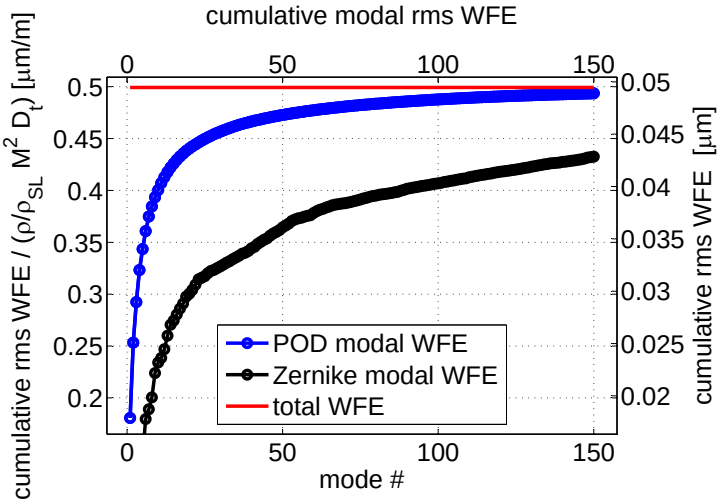

(b)

Figure 6. (a) POD modal rms wavefront error as function of mode number. (b) Cumulative POD modal wavefront error (blue) and Zernike modal wavefront error (black) as function of mode number. The red line shows the total aperture-averaged wavefront error of the entire wavefront sequence.

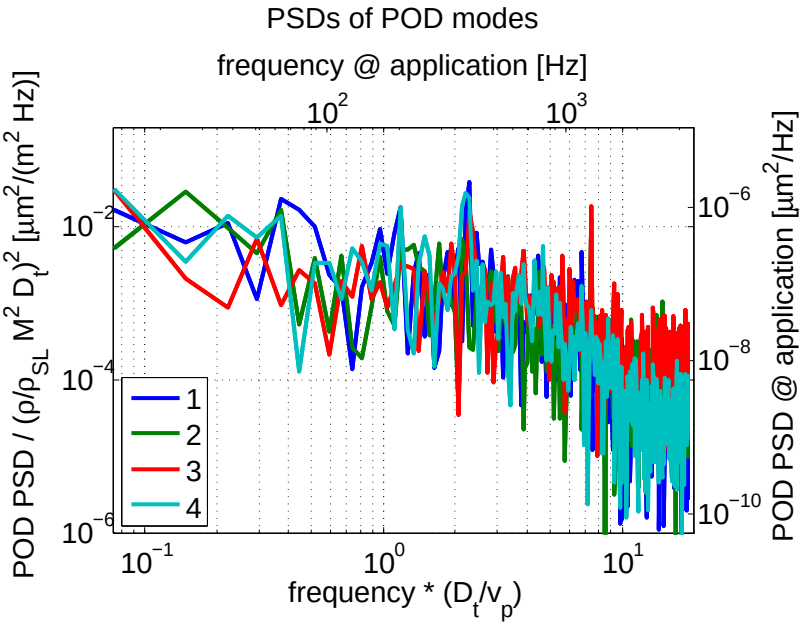

(a)

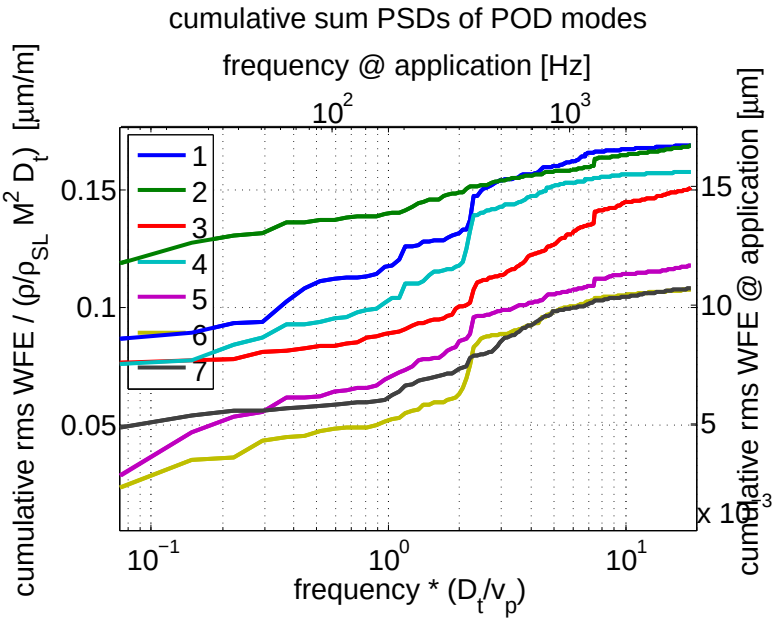

(b)

Figure 7. (a) PSDs of first four POD modes. (b) Cumulative PSDs of first seven POD modes.

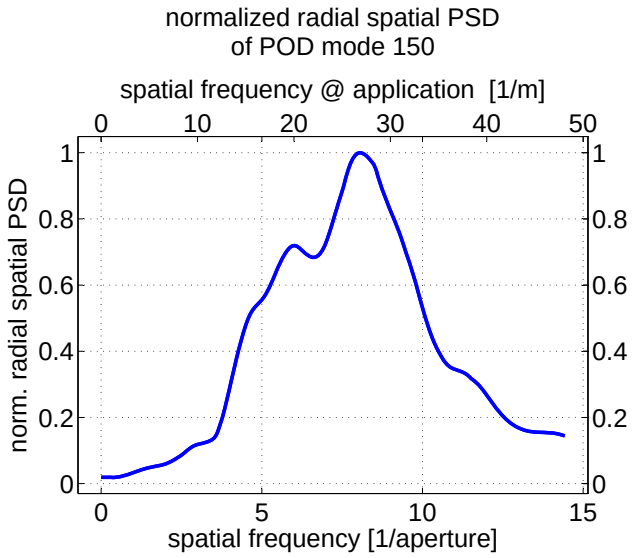

(a)

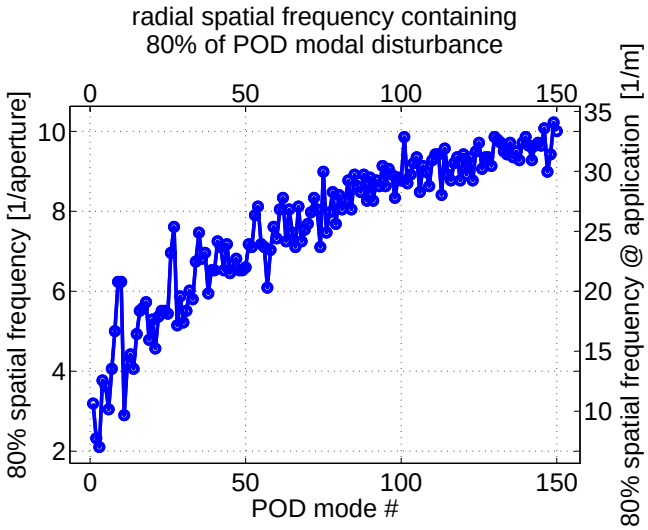

(b)

Figure 8. (a) Normalized radial spatial PSD of 150^{th} POD mode $\Psi^{rad}_{150}(\nu_r)/max(\Psi^{rad}_{150}(\nu_r))$. (b) Maximum spatial frequency content as function of POD mode number $\nu^{max}_{r,k}$.

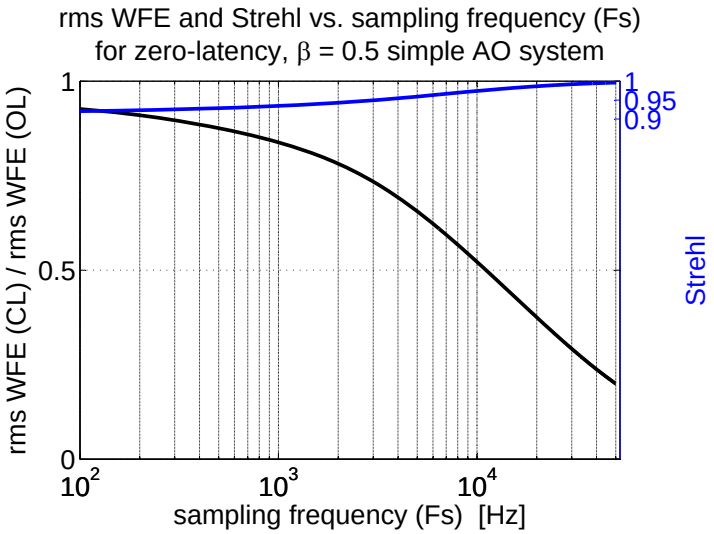

Figure 9. Zero-latency ($\Delta t = 0$) conventional AO control performance versus sample rate f_s for gain of $\beta = 0.5$. Blue curve shows the resulting Strehl (right axis). Black curve shows the normalized residual rms wavefont error (left axis).

B. Mach 0.5, 15 kft, $\alpha = 105^o$ (139^o az., 70^o el.)

Here, we repeat the same analysis from Section A on the Mach 0.5, 15 kft, 139^o az., 70^o el. wavefront sequence. The application scenario is the same as well, except that the azimuth and elevation angles are now different.

1. Wavefront error

The wavefront error statistics for the [139^o az., 70^o el.] wavefront sequence are presented in Table 2 for the "as measured", "non-dimensionalized", and "scaled to application" cases. Comparatively, the the rms wavefront error of this wavefront sequence is significantly *larger* than the rms wavefront error of the [47^o az., 42^o el.] case when scaled to the same application scenario. Figure 13 shows the ensemble rms wavefront error on a pixel-by-pixel bases for both (a) non-dimensionalized wavefronts and (b) wavefronts scaled to the tactical HEL weapon system application scenario given at the beginning of this Section. At larger turret look-back angles, the major aberrations possess a definite flow across the aperture. Here, the flow direction is from bottom-right to top-left in both figures. Notice the large wavefront variance on the trailing end of the aperture that was not present in the [47^o az., 42^o el.] case. This is most likely due to vortex shedding.

	As Measured	Non-Dimensionalized	Scaled to Application
Ap. Avg. Phase Var. [μm^2]	0.005	2.085	0.020
rms WFE [μm]	0.069	1.444	0.143
avg. OPDrms [μm]	0.067	1.410	0.140
avg. OPDp-v [μm]	0.428	9.006	0.892

Table 2. Wavefront error statistics for 15 kft, Mach 0.5, 139^o az., 70^o el.. Units are for "As-Measured" and "Scaled to Application" wavefronts only. Non-dimensionalized wavefronts are unitless.

Figure 13 (a) and (B) show the aperture-averaged pixel PSD and cumulative aperture-averaged pixel PSD for the [139^o az., 70^o el.] wavefront sequence, respectively. Notice that there is a "dip" in the PSD in the region

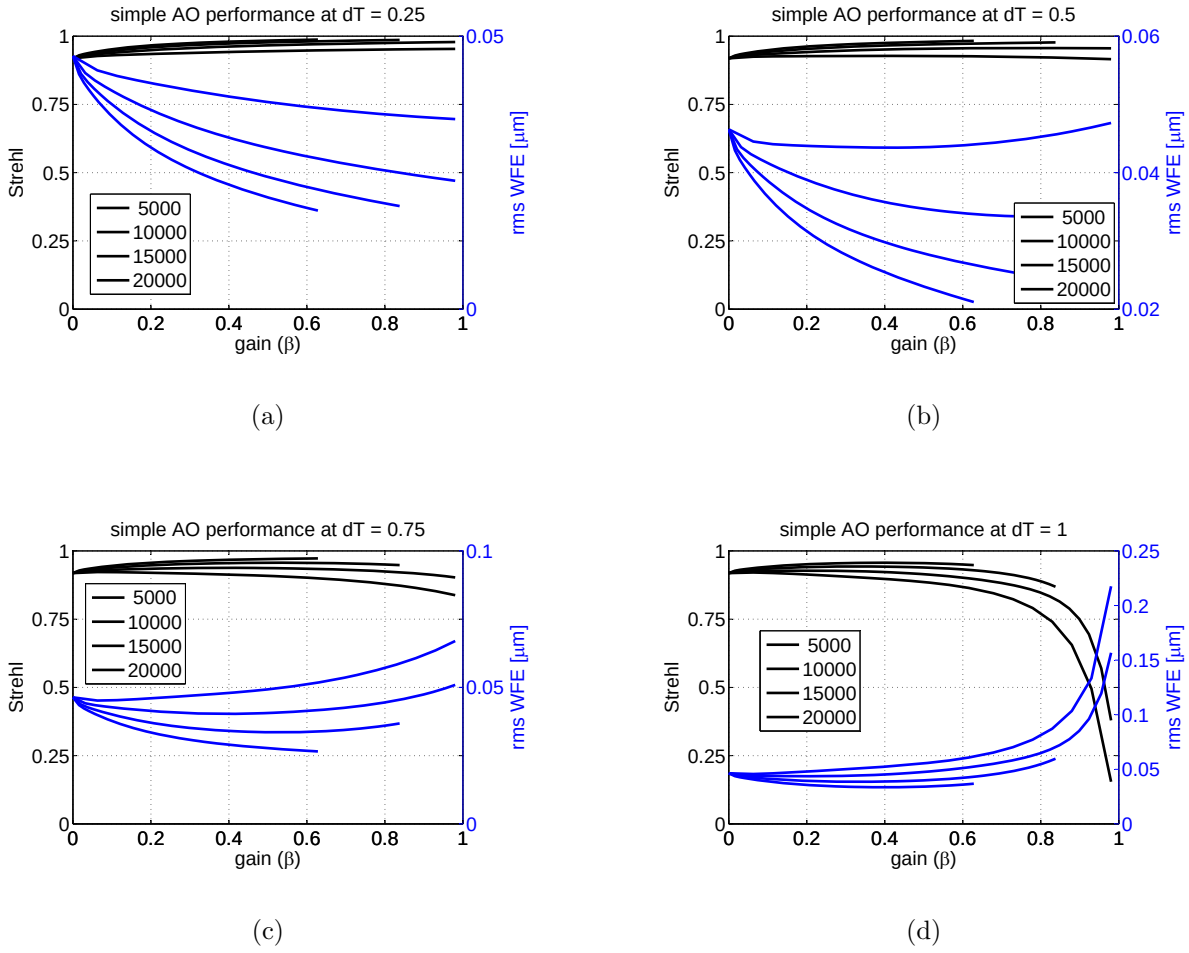

Figure 10. Conventional AO control performance versus gain with different sample rates f_s for (a) 0.25, (b) 0.50, (c) 0.75, and (d) 1.00 frames of latency. Black curves are the resulting Strehl (left axis). Blue curves are the residual rms wavefont error (right axis). In all cases, performance increases with increasing sample rate.

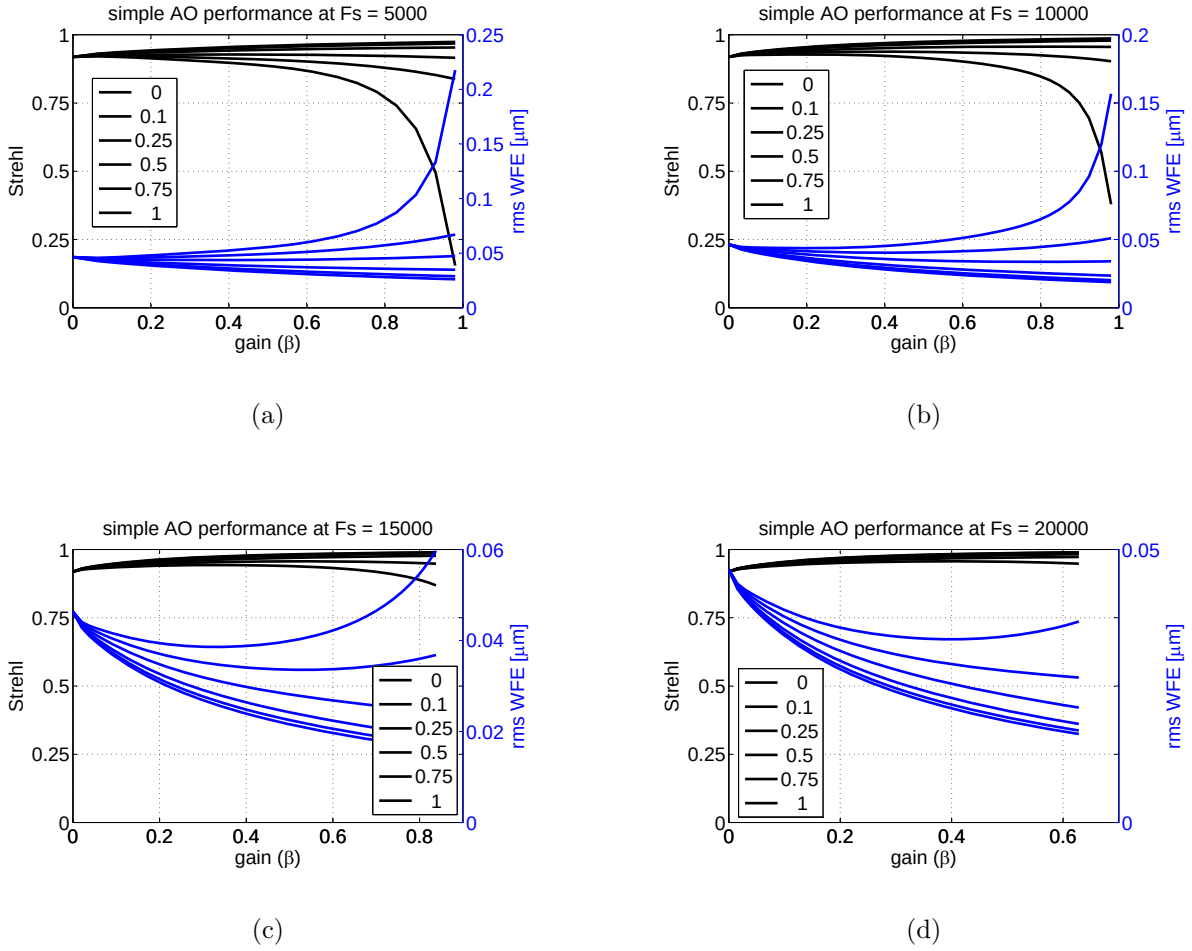

Figure 11. Conventional AO control performance versus gain with different frames of latency Δt for sample rates f_s of (a) 5 kHz, (b) 10 kHz, (c) 15 kHz, and (d) 20 kHz. Black curves are the resulting Strehl (left axis). Blue curves are the residual rms wavefont error (right axis). In all cases, performance increases with decreasing latency.

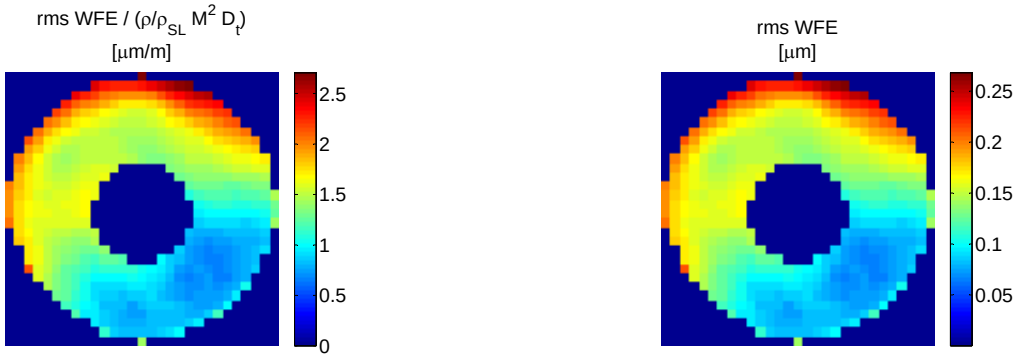

(a) (b)

Figure 12. Ensemble root-mean-square wavefront error (rmsWFE) on a pixel-by-pixel basis for (a) non-dimensionalized wavefronts and (b) wavefronts scaled to the tactical HEL weapon system application scenario.

from about 40 Hz to 400 Hz (for wavefronts scaled to application along top axis) that was not present in the [47^o az., 42^o el.] wavefront sequence. The types of aero-optics disturbances that are likely to be responsible for wavefront variance in this 40 Hz to 400 Hz frequency range are most likely of the "oil-canning" type, where a "blob" moves around the aperture without "passing through" or flowing across as shear layer vortices do.

2. POD modal analysis

The POD modes for the [139^o az., 70^o el.] sequence of wavefronts is displayed in Figure 14. Notice how modes 1,2, 3,4, and 5,6, and are complimentary pairs with the second mode of each pair being a $\pi/2$ phase shift away from the first mode, at least in the trailing half of the aperture. This is a strong indication of shear layer formation and vortex shedding. The [47^o az., 42^o el.] sequence showed some complimentary pairs of POD modes, though not as pronounced as in this case. Interestingly, for the [47^o az., 42^o el.] wavefront sequence, the higher POD modes, e.g. modes 7,8,9,10, show high spatial frequency components that appear complimentary. See Figure 5. Such modal structures have only been observed at the more forward-looking turret window angles. At this point it is not clear to us what the origin of structures is, but it is clear that POD modes can provide a lot of information about the characteristics of the flow, that would not be apparent in Zernike decomposition analysis.

Figure 15 shows (a) the rms wavefront error contribution of each POD mode and (b) the cumulative sum (over mode number) of the POD modal rms wavefront error compared to the Zernike modal rms wavefront error. Clearly, as we pointed out above, the Zernike modes are unable to capture the true wavefront error due to the non-isotropic nature of these aero-optics disturbances.

The PSDs and cumulative sum PSDs of the first few POD modal coefficients are plotted in Figure 16 (a) and (b), respectively. Comparatively, the main difference between the POD PSDs of the [47^o az., 42^o el.] and [139^o az., 70^o el.] sequences of wavefronts is that the wavefront variance is diminished from 40 Hz to 400 Hz in the "scaled-to-application" case (top and right axes) for the [139^o az., 70^o el.] sequence and is relatively flat over the same interval for the [47^o az., 42^o el.] sequence. Also, here, the cumulative sum PSDs have a steeper rise compared to the more gradual rise observed with the [47^o az., 42^o el.] wavefront sequence. See Figure 16 for comparison.

3. Spatial frequency content

In looking at the spatial frequency content of the [139^o az., 70^o el.] versus the [47^o az., 42^o el.] wavefront sequences, we find that they are nearly the same, at least the the radial direction (with averaging over angle). This can be see by comparing Figure 17(b) with Figure 8(b). In both cases, we estimate the number of DM actuators needed to compensate up to 100 POD modes, for example, to be $2 \times \nu_{r,100}^{max} = 2 \times 9 = 18$ actuators

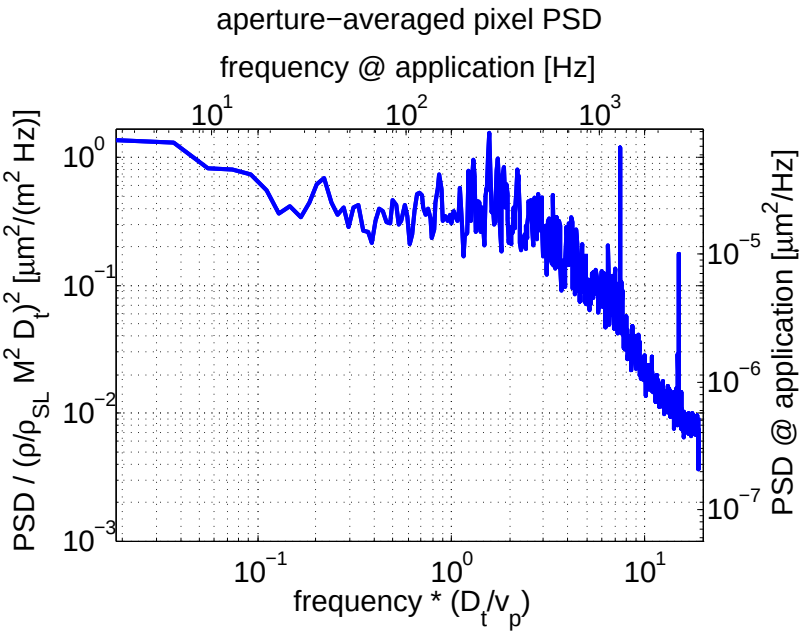

(a)

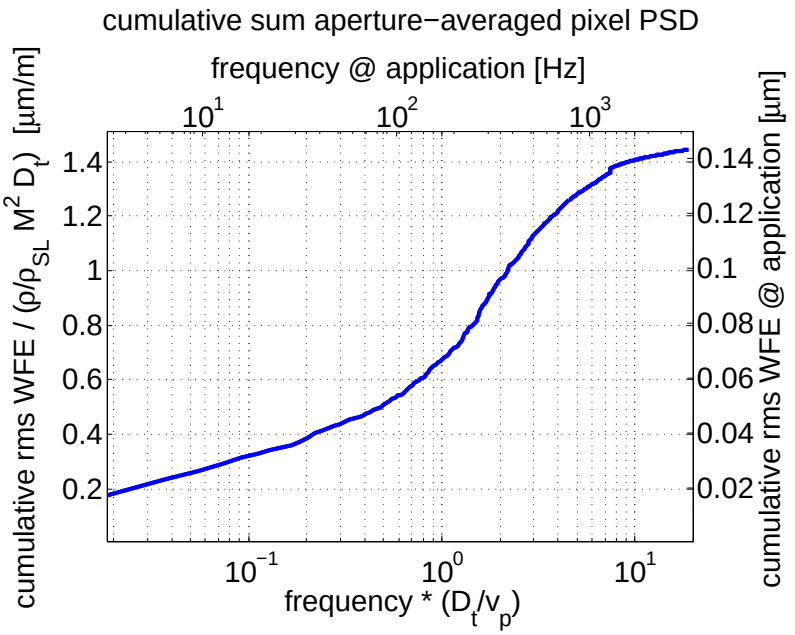

(b)

Figure 13. (a) Aperture-averaged pixel PSD. (b) Cumulative aperture-averaged pixel PSD.

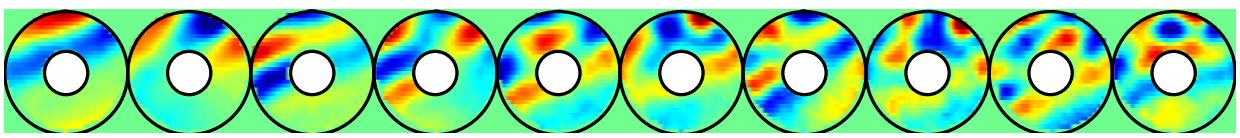

Figure 14. First 10 POD modes.

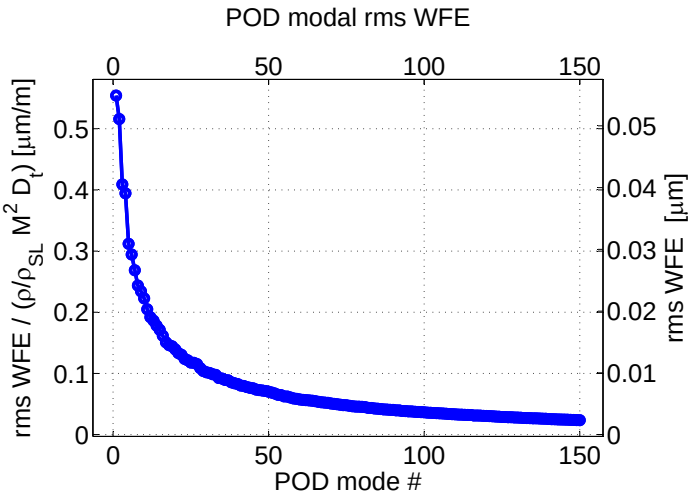

(a)

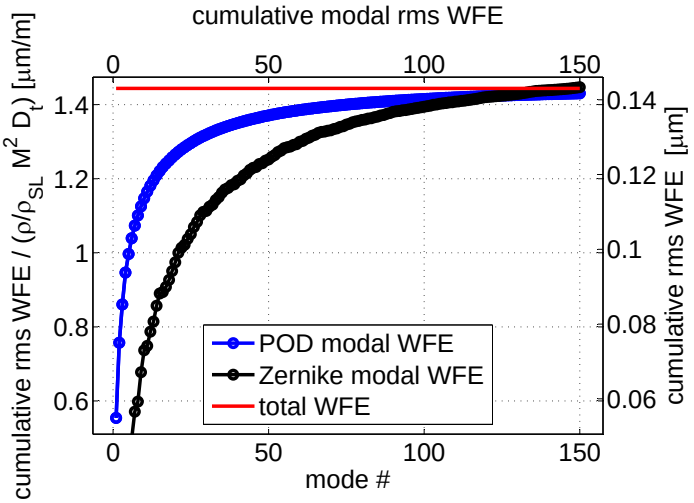

(b)

Figure 15. (a) POD modal rms wavefront error as function of mode number. (b) Cumulative POD modal wavefront error (blue) and Zernike modal wavefront error (black) as function of mode number. The red line shows the total aperture-averaged wavefront error of the entire wavefront sequence.

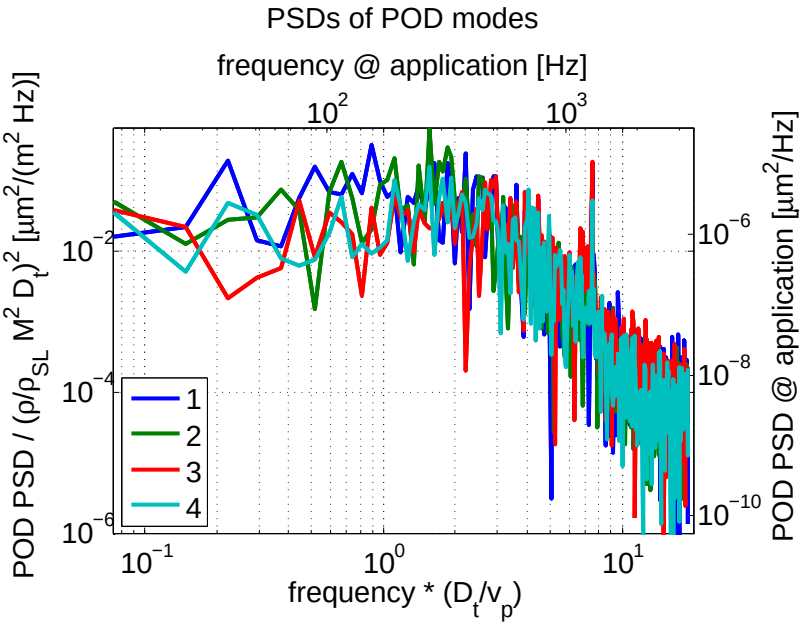

(a)

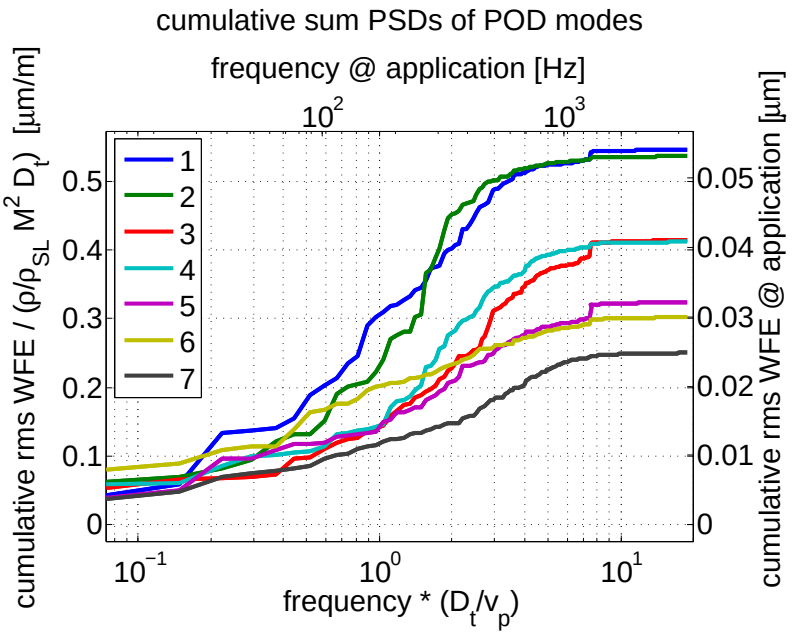

(b)

Figure 16. (a) PSDs of first four POD modes. (b) Cumulative PSDs of first seven POD modes.

across the aperture. Thus there is not a significant difference between the two wavefront sequences in terms of compensation from a spatial point of view.

4. Conventional AO compensation performance

One of the striking differences between the [139^o az., 60^o el.] and [47^o az., 42^o el.] wavefront sequences scaled to the same application scenario, is their respective susceptibility to mitigation from a simple integrator type conventional AO controller. Figure 18 shows the zero-latency ($\Delta t = 0$ frames) Strehl ratio and rms wavefront error for the [139^o az., 70^o el.] wavefront sequence as a function of AO controller sample rate f_s for a gain of $\beta = 0.5$. Already we can see that the open-loop Strehl is significantly lower than the open-loop Strehl for the [47^o az., 42^o el.] case. Also, the Strehl only rises above 50% after the AO system is running over 1 kHz sample rate.

Figure 19 and Figure 20 show plots of conventional AO controller performance against the [139^o az., 70^o el.] wavefront sequence for the same conditions as shown in Figure 10 and Figure 11 for the [47^o az., 42^o el.] wavefront sequence. Consider a 1 frame latency AO system. Figure 19(d) shows that when the sample rate is less than or equal to 10 kHz, performance is always worse than open-loop. Of course, if the latency were to be reduce, the minimum sample rate necessary to yield a performance better than open-loop is reduced. For example, Figure 19(b) shows that a latency of half a frame would result in Strehl increases over open-loop as long as the sample rate was at least 5 kHz.

IV. Conclusions

Using *in-flight* AAOL wavefront measurements of aero-optical disturbances for two turret window angles (one forward-looking and one rear-looking), scaled to a relevant tactical airborne HEL weapon system scenario and analyzed according to POD mode spatial and temporal power spectral densities, the potential implications for AO beam control were examined. It was found that, left uncorrected, the rear-looking aero-optics at such flight conditions would cause a significant degradation in Strehl whereas the forward-looking wavefronts, although possessing large high-frequency content, would result in milder Strehl degredations. These aero-optics wavefronts were highly directional lacking radial symmetry thereby rendering conventional Zernike analysis unfit for use. POD analysis proved to be more useful in both describing the characteristics of the flow and in evaluation of spatial and temporal requirements for an AO system in dealing with aero-optics disturbances. In terms of the spatial requirements of an adaptive optics system in compensating such disturbances, it was found that only about 18 DM actuators would be required to effectively compensate either one of the two wavefront sequences ([139^o az., 70^o el.] and [47^o az., 42^o el.]) as no significant variation in radial spatial frequency content versus POD mode number was observed between the two sequences. Current commercial DM and wavefront sensor (WFS) AO hardware is capable of achieving such spatial resolution. However, the temporal requirements imposed upon an AO control system are much more stringent in terms of latency and sample rate, in particular for the rear-looking turret case. It was found that there was a large difference between the two wavefront sequences, scaled to the same airborne tactical HEL weapon system application scenario. In particular, the wavefront error of the [139^o az., 70^o el.] sequence was nearly three times greater than that of the [47^o az., 42^o el.] sequence. However, the temporal requirements of an AO system to preform better than open-loop was similar. Generally, sample rates in excess of 10 kHz would be necessary with a one-frame-of-latency AO control system in order to produce Strehl ratios greater than open-loop. Consequently, the main route toward improving aero-optics Strehl lies in reducing the latency of an AO control system. Improved control algorithms such as adaptive and predictive control show promise for effectively reducing the latency AO control loop which will most likely be necessary for effective mitigation of aero-optics in airborne tactical HEL weapons.

Acknowledgments

This work was sponsored by AFOSR, Air Force Material Command, USAF under Grant Number FA9550-07-1-0574. The U.S. Governments is authorized to reproduce and distribute reprints for governmental purposes notwithstanding any copyright notations hereon.

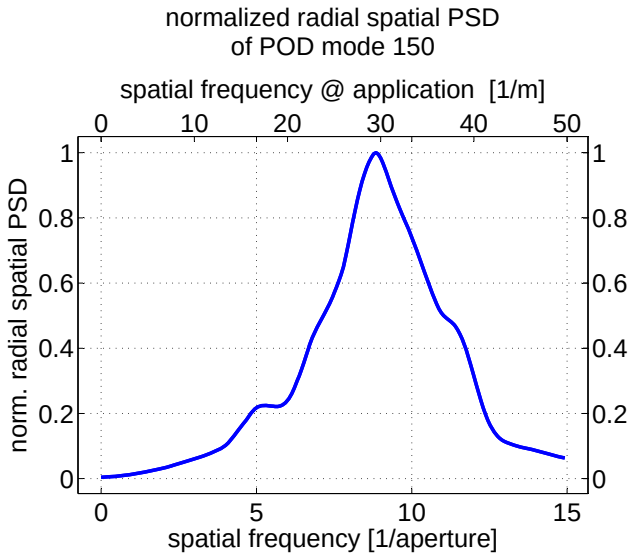

(a)

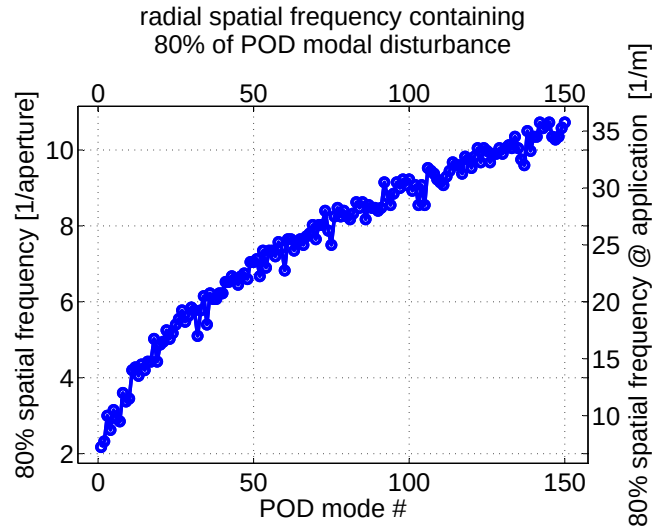

(b)

Figure 17. (a) Normalized radial spatial PSD of 150^{th} POD mode $\Psi_{150}^{rad}(\nu_r)/max(\Psi_{150}^{rad}(\nu_r))$. (b) Maximum spatial frequency content as function of POD mode number $\nu_{r,k}^{max}$.

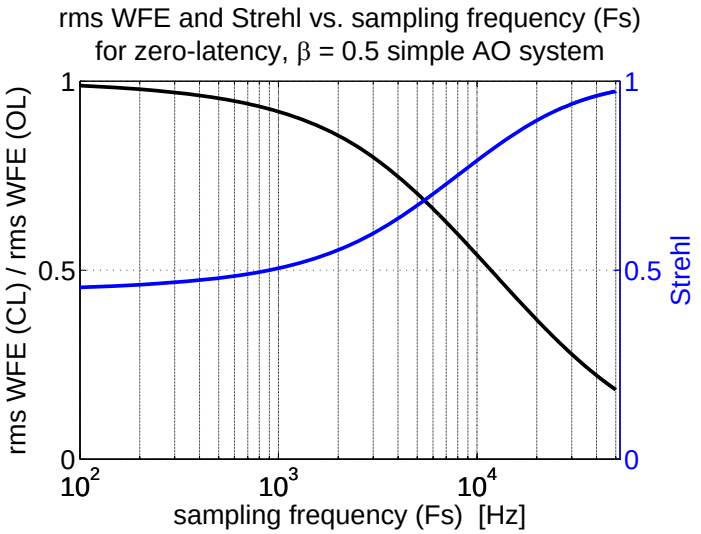

Figure 18. Zero-latency ($\Delta t = 0$) conventional AO control performance versus sample rate f_s for gain of $\beta = 0.5$. Black curve shows the resulting Strehl (left axis). Blue curve shows the residual rms wavefont error (right axis).

References

[1]Wittich, D. J., Gordeyev, S., and Jumper, E. J., "Revised Scaling of Optical Distortions Caused by Compressible, Subsonic Turbulent Boundary Layers," *38th AIAA Plasmadynamics and Lasers Conference*, Vol. 4009, 2007.

[2]Gordeyev, S., Hayden, T., and Jumper, E. J., "Aero-Optical and Flow Measurements over a Flat-Windowed Turret," *AIAA Journal*, Vol. 45, No. 2, 2007, pp. 347–357.

[3]Gordeyev, S. and Jumper, E., "Fluid Dynamics and Aero-Optical Environment Around Turrets," *40th AIAA Plasmadynamics and Lasers Conference*, June 2009.

[4]Gordeyev, S. and Jumper, E., "Fluid dynamics and aero-optics of turrets," *Prog. Aerospace Sci.*, Vol. 46, 2010, pp. 338–400.

[5]Kyrazis, D. T., "Optical degradation by turbulent free-shear layers," *Proc. SPIE: Optical Diagnostics in Fluid and Thermal flow*, edited by S. S. Cha and J. D. Trolinger, Vol. 2005, 1993, pp. 170–181.

[6]S.V., G., *Ph.D. Dissertation: Investigation of Coherent Structure in the Self-Similarity Region of the Turbulent Planar Jet Using POD and Wavelet Analysis*, University of Notre Dame, Notre Dame, IN, 1999.

[7]Chatterjee, A., "An introduction to the proper orthogonal decomposition," *Current Science*, Vol. 78, No. 7, April 2000, pp. 808–817.

[8]S.V., G. and F.O., T., "Coherent Structure in the Turbulent Planar Jet. Part 1. Extraction of Proper Orthogonal Decomposition Eigenmodes and Their Self-Similarity," *Journal of Fluid Mechanics*, Vol. 414, 2000, pp. 145–194.

[9]S.V., G. and F.O., T., "Coherent Structure in the Turbulent Planar Jet. Part 2. Structural Topology via POD Eigenmode Projection," *Journal of Fluid Mechanics*, Vol. 460, 2002, pp. 349–380.

[10]Rennie, R. M., Duffin, D. A., and Jumper, E. J., "Characterization and Aero-Optic Correction of a Forced Two-Dimensional, Weakly-Compressible Subsonic Free Shear Layer," *AIAA Journal*, Vol. 46, No. 11, 2008, pp. 2787–2795.

[11]Gordeyev, S. and Thomas, F., "A Temporal Proper Orthogonal Decomposition (TPOD) Method for Closed-Loop Flow Control," *AIAA 2010-0359*, January 2010.

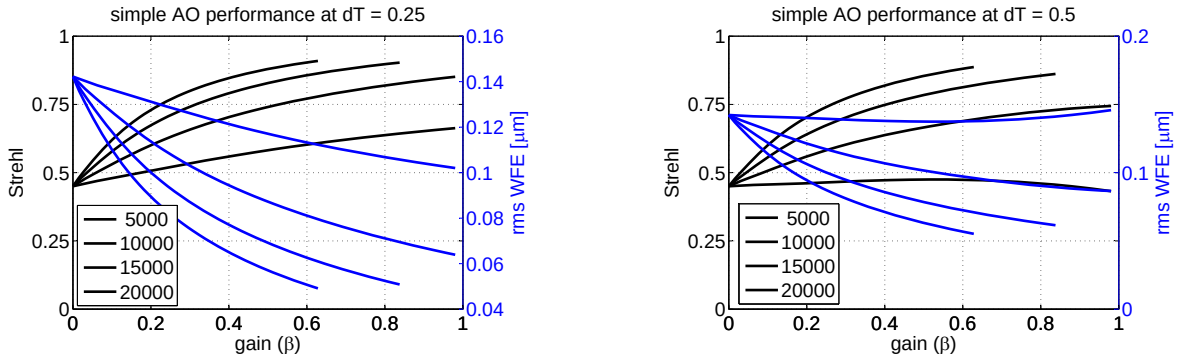

(a)

(b)

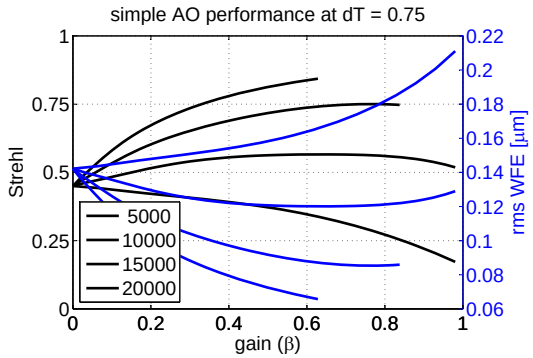

(c)

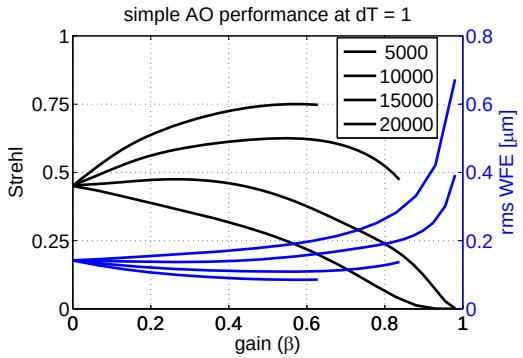

(d)

Figure 19. Conventional AO control performance versus gain with different sample rates f_s for (a) 0.25, (b) 0.50, (c) 0.75, and (d) 1.00 frames of latency. Black curves are the resulting Strehl (left axis). Blue curves are the residual rms wavefont error (right axis). In all cases, performance increases with increasing sample rate.

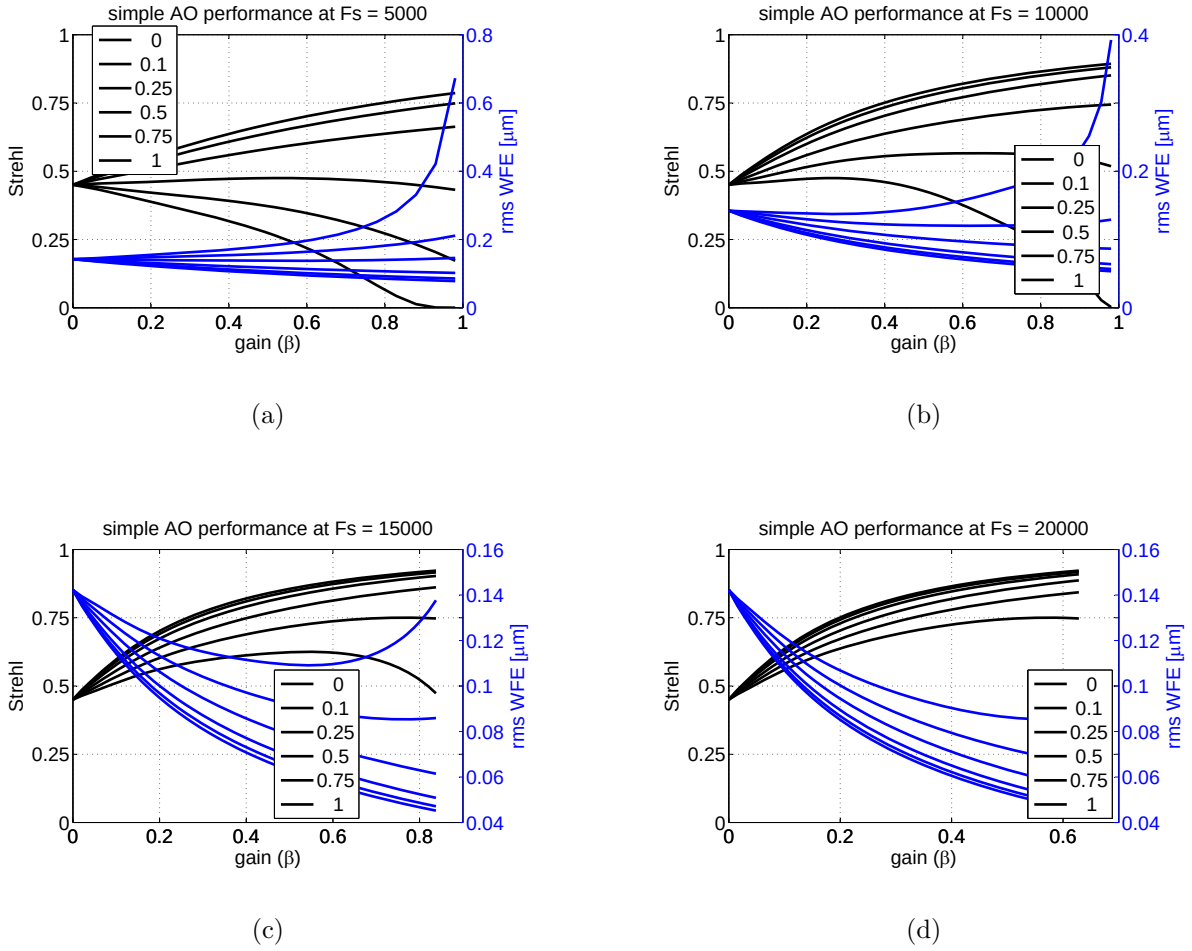

Figure 20. Conventional AO control performance versus gain with different frames of latency Δt for sample rates f_s of (a) 5 kHz, (b) 10 kHz, (c) 15 kHz, and (d) 20 kHz. Black curves are the resulting Strehl (left axis). Blue curves are the residual rms wavefont error (right axis). In all cases, performance increases with decreasing latency.

List of Abbreviations

AAOL	Airborne Aero-Optics Laboratory
AFOSR	Air Force Office of Scientific Research
AO	adaptive optics
DM	deformable mirror
ELLA	Electric Laser on Large Aircraft
HEL	high energy laser
OPL	optical path length
OPD	optical path difference
POD	proper orthogonal decomposition
PSD	power spectral density
WFS	wavefront sensor